



Direct observation of water-mediated single-proton transport between hBN surface defects

Jean Comtet¹✉, Benoit Grosjean², Evgenii Glushkov¹, Ahmet Avsar^{3,4}, Kenji Watanabe⁵, Takashi Taniguchi⁵, Rodolphe Vuilleumier², Marie-Laure Bocquet² and Aleksandra Radenovic¹✉

Aqueous proton transport at interfaces is ubiquitous and crucial for a number of fields, ranging from cellular transport and signalling, to catalysis and membrane science. However, due to their light mass, small size and high chemical reactivity, uncovering the surface transport of single protons at room temperature and in an aqueous environment has so far remained out-of-reach of conventional atomic-scale surface science techniques, such as scanning tunnelling microscopy. Here, we use single-molecule localization microscopy to resolve optically the transport of individual excess protons at the interface of hexagonal boron nitride crystals and aqueous solutions at room temperature. Single excess proton trajectories are revealed by the successive protonation and activation of optically active defects at the surface of the crystal. Our observations demonstrate, at the single-molecule scale, that the solid/water interface provides a preferential pathway for lateral proton transport, with broad implications for molecular charge transport at liquid interfaces.

Proton transport in bulk water is known to occur via the so-called Grotthuss mechanism¹, whereby protons tunnel between individual water molecules along liquid wires formed by hydrogen bonds. This remarkable transport mechanism, postulated almost 200 years ago, explains the anomalous and peculiarly high mobility of hydronium and hydroxide ions in bulk water². At interfaces, the situation is much more complex, with experimental and theoretical efforts pointing to a wealth of effects, ranging from specific proton desorption barriers³ potentially facilitated by interactions with water molecules⁴ and hydrogen bonding^{5–7}, peculiar charging effects due to water negative self-ion⁸, to two-dimensional (2D) confinement of protons at hydrophobic interfaces, leading to facilitated lateral transport^{9–12}. However, interfacial transport of protons, and its relationship with the surrounding aqueous water environment has so far remained elusive, due to a lack of direct measurements at the single-molecule scale and under environmental conditions. A finer molecular understanding of proton transport at interfaces would have fundamental importance for a range of fields and materials, from cell membranes in biology^{9–12}, metallic and oxide surfaces for catalysis and surface science^{4,13–15}, to polymeric surfaces for fuel cells^{16–20} and membrane science^{21–24}.

Here, we use single-molecule localization microscopy to resolve the transport of individual excess protons between defects at the surface of hexagonal boron nitride (hBN) crystals in contact with water. Our label-free approach relies on the protonation-induced optical activation of defects at the surface of the flake. Building upon the recent application of super-resolution microscopy to hBN defects^{25,26}, we are able to follow spatial trajectories of individual excess protons through successive hopping and activation of surface defects. We reveal heterogeneous water-mediated proton

mobility under illumination, with proton transport limited by desorption from individual defects. Our observations demonstrate that the solid/water interface provides a preferential pathway for proton and charge transport. This finding, along with the chemical nature of the defects in aqueous conditions, is corroborated by full quantum molecular dynamic simulations of pristine and defective hBN/water interfaces. Our findings and observations have general implications for proton transport between titratable surface groups or surface traps, as can arise at a variety of biological^{9,11,27} and solid-state^{3,13,16,18,28} interfaces.

Reactivity of hBN surface defects in aqueous conditions

As shown in Fig. 1a, our sample is composed of multilayer boron nitride flakes, exfoliated from high-quality crystals²⁹. Such exfoliated hBN flakes are atomically smooth and host very few intrinsic defect sites³⁰. Defects are deterministically induced at the surface of the flake through a brief low-power oxygen plasma treatment^{26,31} (Supplementary Discussion 1.4). Wide-field illumination of the sample with a continuous green laser ($\lambda_{\text{exc}} = 561 \text{ nm}$) leads to localized emission from optically active defects at the surface of the flake, which is characterized by uniform emission at 585 nm (2.08 eV), consistent with previous reports^{26,32} (Supplementary Fig. 1).

Remarkably, as shown in Fig. 1b–d, we observe a drastic change in the photoluminescence response of the hBN flake when exposed to air ((i), black) or to aqueous solutions of varying acidity ((ii), blue, and (iii), red, corresponding to pH 9.8 and pH 3.4, respectively), pointing to the high reactivity of surface defects in aqueous conditions. Figure 1b shows the wide-field image of the hBN flake under uniform illumination, with the flake physical boundary highlighted as a white contour. For each frame, emission originating

¹Laboratory of Nanoscale Biology, Institute of Bioengineering, School of Engineering, École Polytechnique Fédérale de Lausanne (EPFL), Lausanne, Switzerland. ²PASTEUR, Département de chimie, École normale supérieure, PSL University, Sorbonne Université, Paris, France. ³Electrical Engineering Institute, École Polytechnique Fédérale de Lausanne (EPFL), Lausanne, Switzerland. ⁴Institute of Materials Science and Engineering, École Polytechnique Fédérale de Lausanne (EPFL), Lausanne, Switzerland. ⁵National Institute for Materials Science, Tsukuba, Japan. ✉e-mail: jean.comtet@gmail.com; aleksandra.radenovic@epfl.ch

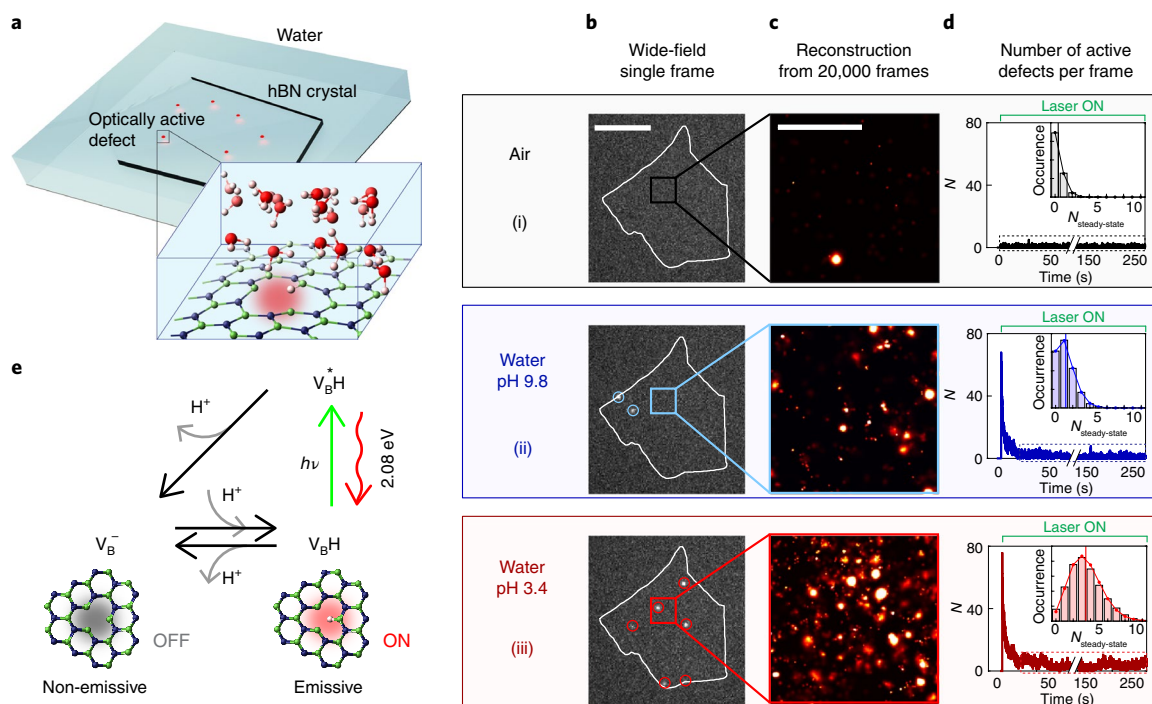


Fig. 1 | Reactivity of hBN defects in aqueous conditions: protonation activates defects. **a**, hBN crystal containing irradiation-induced surface defects is illuminated by a continuous green laser, leading to localized emission from optically active defects (red). The crystal can be exposed to various environmental conditions (air, or water solutions of varying acidity). Inset: zoomed-in view of a surface defect (protonated boron vacancy V_BH), surrounded by water molecules. Boron, nitrogen, oxygen and hydrogen atoms are represented as blue, green, red and white, respectively. **b–d**, Larger defect reactivity in aqueous acidic conditions, comparing flake in (i) air, (ii) in basic (pH 9.8) and (iii) acidic (pH 3.4) water solutions. **b**, Wide-field image of an hBN flake, obtained with 20 ms exposure time. Emission from individual surface defects (highlighted by red and blue circles) can be localized with $\sim 5\text{--}40$ nm uncertainty (see Supplementary Discussion 1.2). Scale bar, $5\ \mu\text{m}$. **c**, Reconstructed super-resolved images of the flake surface (Supplementary Discussion 1.3). Scale bar, $1\ \mu\text{m}$. **d**, Number, N , of emissive defects per frame as a function of time for the three environmental conditions. In air, the number of active defects is consistently small. In water, we observe a large number of active defects upon illumination, which decreases to reach a steady state (dashed box, see Supplementary Discussion 2 and Supplementary Fig. 5 for analysis of the relaxation kinetics). Inset shows the histogram of the number of active defects per frame at steady state, $N_{\text{steady-state}}$ fitted by Poisson distributions. Vertical lines in the inset show the average number of defects per frame. A larger activity of surface defects is evidenced in acidic conditions, consistent with protonation-induced activation of defects. **e**, Three-state model for the protonation-induced transition between non-emissive negatively charged boron vacancy V_B^- , and emissive neutral protonated boron vacancy V_BH , with excited state V_B^+H (Supplementary Fig. 4).

from surface defects can be localized with subwavelength uncertainty, with a typical localization uncertainty $\sigma_{\text{LOC}} \approx 5\text{--}40$ nm, scaling as $\sigma_{\text{LOC}} \approx \sigma_{\text{PSF}} / \sqrt{N_\phi}$, with $\sigma_{\text{PSF}} \approx 150$ nm fixed by the point spread function of the microscope and N_ϕ , the number of emitted photons (Fig. 1b, blue and red circles show localized defects, also see Supplementary Discussion 1.2). Consecutive localization of emitters over successive frames (here 20,000) allows us to reconstruct a super-resolved spatial map of the defects at the surface of the crystal^{25,26}, with a zoomed-in view on a $2 \times 2\ \mu\text{m}^2$ area shown in Fig. 1c. We observe, in Fig. 1c, that while only few defects are active in air, a large number of defects are homogeneously activated in aqueous conditions (Supplementary Fig. 9 for super-resolved maps of the entire flake). This difference is also highlighted by monitoring the number, N , of emissive defects per frame under illumination (Fig. 1d). In air, the number of active defects per frame is consistently low, with $\langle N \rangle \approx 0.3$ active defects per frame. Immersing the flake in water, we observe upon illumination a very large number of active defects (here $N \approx 70$, corresponding to ~ 1 active site per μm^2), pointing to the activation of defect luminescence due to solvent molecules (Supplementary Fig. 9). The number of active defects decreases upon illumination over tens of seconds (Supplementary Figs. 3 and 5) to reach a steady state, characterized by $\langle N \rangle \approx 1\text{--}4$ active defects per frame. Importantly, the luminescent state of defects is recovered over sufficiently long dark periods, as well

as through successive drying and wetting steps (Supplementary Figs. 6 and 7).

Varying water acidity further allows us to identify environmental protons, H^+ , as being the chemical species responsible for the activation of defect luminescence. Comparing the two pH conditions in Fig. 1b–d, we indeed observe an increase by a factor of ~ 2 in the number of emissive defects at acidic pH (Fig. 1d, inset), as well as an increase in the density of activated emitters (Fig. 1c). This monotonic increase in defect activity under acidic conditions was systematically observed in all the investigated crystals over 12 pH units (Supplementary Fig. 10).

To rationalize our observations, we perform ab initio molecular dynamic simulations of a defective hBN interface in water (Fig. 1a, inset, Supplementary Discussion 5 and Supplementary Video 1). On the basis of recent simulations on anhydrous bulk hBN defects³³ and high-resolution transmission electron microscopy images of hBN monolayers^{25,34}, we probed the reactivity of boron monovacancy complexes in water, namely, V_BH (identified as the likely 2 eV emitter³³) and V_B^- (non-emissive at 2 eV, having a lower acceptor defect state in the gap). Our simulations demonstrate that solvated aqueous protons behave like charge-compensating centres and incorporate easily on the negatively charged defect V_B^- , through $V_B^- + H^+ \Rightarrow V_BH$, which is consistent with the large activation of luminescence observed in the aqueous environment.

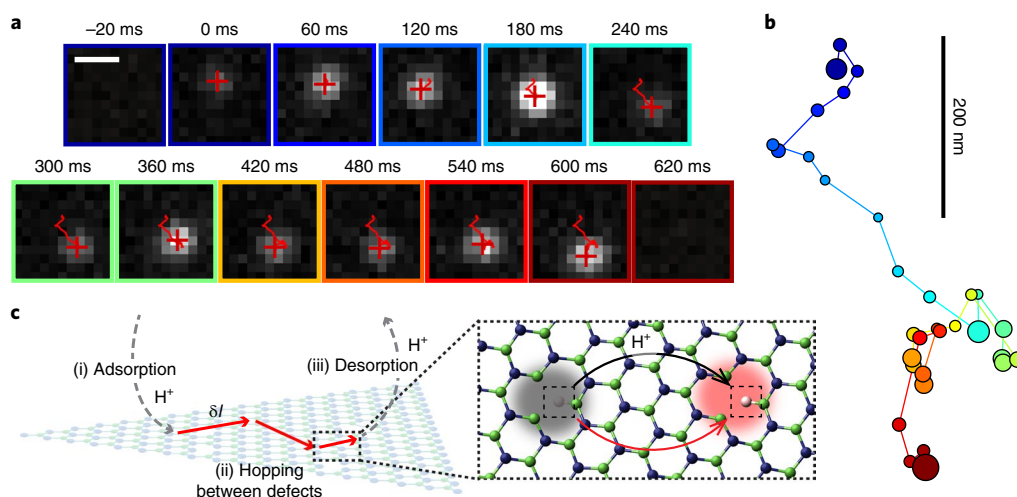


Fig. 2 | Luminescence migration reveals proton trajectories. **a**, Time series for spatial migration of luminescence at the surface of the flake, with wide-field images showing the localized diffraction-limited spot at the surface of the flake (red cross) and reconstructed spatial trajectory in red (Supplementary Video 3). Scale bar, 500 nm. Projected pixel size is 100 nm. **b**, Reconstructed trajectories showing successive activation of adjacent defects at the surface of the flake and colour-coded with increasing time. Localized defects are represented as dots, with the radius corresponding to the localization uncertainty. **c**, Schematic depicting luminescence migration events, consisting of successive (i) proton adsorption (appearance of a luminescence spot at the surface of the flake), (ii) excess proton hopping between surface defects (diffusion of the luminescence spot) and (iii) proton desorption from the surface of the flake (disappearance of the luminescence spot).

These numerical observations allow us to propose the phenomenological three-state model depicted in Fig. 1e. In the absence of illumination, the number of protonated defects is fixed by the acid–base equilibrium $V_B^- + H^+ \rightleftharpoons V_BH$. Probing this equilibrium experimentally, we determine a $pK_a \geq 14$, consistent with the strong basicity evidenced by the simulations (Supplementary Fig. 8). Upon illumination, defects in the protonated state are converted to their excited state V_B^+H , from which they can either decay radiatively back to the ground state V_BH , or lose their protons to be converted back to V_B^- , through an excited-state proton transfer³⁵ (Supplementary Fig. 4). This second non-radiative pathway leads to the initial decrease of the number of active defects upon illumination (Fig. 1d and Supplementary Fig. 5) by effectively shifting the chemical equilibrium between V_B^- and V_BH , reaching a second steady-state level under constant laser illumination. This photoacidic behaviour is consistent with the relative excited-state energy levels of the protonated and deprotonated defect³³ (Supplementary Fig. 4). Consistently, a decrease in the number of active defects at steady state is observed for increasing illumination power (Supplementary Fig. 11). This ON/OFF transition between distinct protonation states, reported here for defects in hBN, is commonly observed for fluorescent dyes^{36,37}. Note, finally, that while our observations and ab initio simulations are consistent with the V_BH/V_B^- transition between emissive and non-emissive states, other types of defects with nitrogen-dangling bonds and distinct protonation states could also be responsible for these observations.

Luminescence migration reveals proton trajectories

Since the defects are emissive in their protonated form, monitoring luminescence events at the surface of the flake allows us to directly track down the spatiotemporal dynamics of defect protonation. Figure 2a shows the temporal evolution over 600 ms of the luminescence in a $1 \times 1 \mu\text{m}^2$ region at the surface of a flake immersed in de-ionized water (pH ~ 5.5), with subpixel localization of the position of the emitter shown as the red cross. As highlighted in this sequence of images, a single diffraction-limited luminescence spot spatially wanders between successive frames over a total distance of ~ 500 nm. Consecutive localizations allow us to reconstruct the

position of successively activated defects, shown as the red line trace in Fig. 2a and the reconstructed trajectory in Fig. 2b, with a radius corresponding to uncertainty in localizations. The observation of the consecutive activation of luminescence of nearby defects over 30 successive frames points to the presence of a single activating excess proton hopping from defect to defect (Fig. 2c, inset), and leading to the observed spatiotemporal activation of luminescence. Importantly, monitoring defect activation over the whole flake allows us to discard artefacts in these observed trajectories related to stage drift or random activation of emitters (Supplementary Figs. 14 and 15). As schematically represented in Fig. 2c, this observed sequence of correlated luminescence events must then correspond to (i) the adsorption of a proton at the site of one defect, leading to the appearance of a luminescence spot at the surface of the flake (Fig. 2a, $t=0$ ms), followed by (ii) hopping of the excess proton between nearby surface defects over the total residence time T_R , with successive hopping length δl and (iii) the desorption of the proton from the flake surface, leading to extinction of luminescence (Fig. 2a, $t=620$ ms). Importantly, we demonstrate through simulations that such correlated luminescence events and trajectories cannot stem from the random activation of emitters at the surface, and must correspond to the correlated transfer of single excess proton between defects (Supplementary Discussion 3.2). Following the three-state model of Fig. 1e, the variation in luminescence intensity observed between successive frames could stem from fluctuations between radiative and non-radiative recombination of the excited defects, for example, due to transient proton unbinding and geminate recombination³⁵. Albeit in a different context, the concepts presented here for single-proton tracking are similar to strategies explored in single-molecule and single-enzyme catalysis^{38–40}.

Interfacial mobility and desorption-limited transport

These correlated proton trajectories occur consistently and repeatedly upon constant illumination (Supplementary Video 2). We track and analyse their dynamics using standard single-particle tracking techniques⁴¹, focusing on the steady-state regime with a constant averaged density of active defects per frame of ~ 0.1 –1 per $10 \mu\text{m}^2$ (Fig. 1d, dashed boxes). Individual trajectories are defined

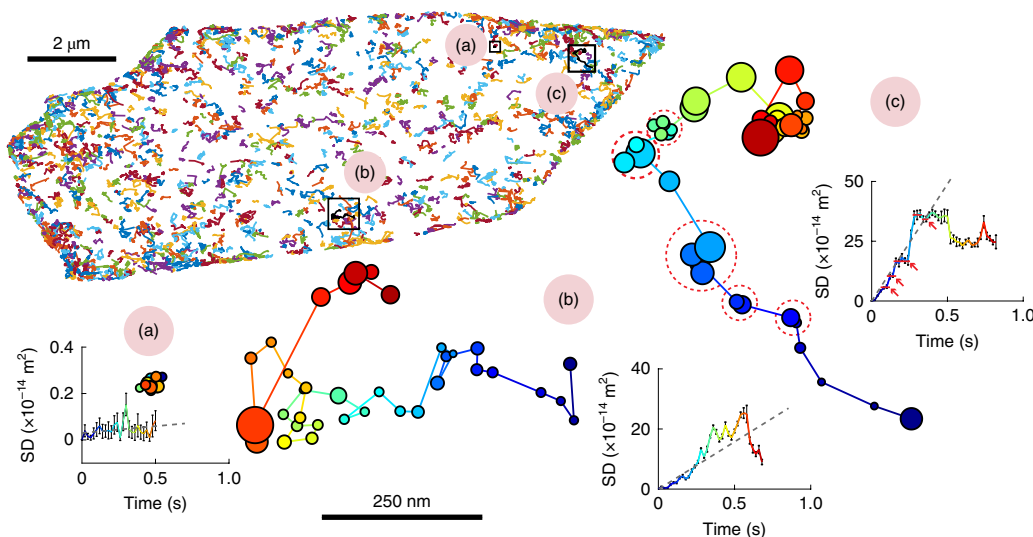


Fig. 3 | Large-scale mapping of proton trajectories. Trajectories longer than ten frames (200 ms) measured at the surface of the flake. Representative trajectories (a)–(c) are highlighted, with the corresponding evolution of the square displacement (SD) (Supplementary Videos 4–6). Defect positions are rendered as circles with a radius corresponding to the localization uncertainty. Black dashed line is a linear fit of the SD for the first 300 ms. For (c), the dashed red circles in the trajectory and the red arrows in the SD show adsorbing steps at some defect sites.

by correlating localizations less than ~ 300 nm apart between successive time frames. This threshold is rigorously defined by measuring the statistic of hopping length δl (Supplementary Fig. 13). Importantly, this tracking methodology is robust with respect to the correlation length and sampling time and is validated against simulations of random activation of emitters (Supplementary Fig. 14). As shown in Fig. 3, ~ 1700 individual trajectories longer than 200 ms (ten successive frames) can be successfully identified over 180 s (Supplementary Video 2). Representative trajectories are highlighted in Fig. 3a–c (see also Supplementary Fig. 19 and Supplementary Videos 4–8). Remarkably, a large heterogeneity is observed between distinct trajectories at the single-molecule scale. Some excess protons remain at a fixed position (Fig. 3a), while others migrate up to $1 \mu\text{m}$ (Fig. 3b,c and Supplementary Fig. 19). Long adsorbing steps (40–100 ms) within one uncertainty-limited defect, separated by relatively long hopping events (50–200 nm), are also observed in some trajectories (red dashed circles, Fig. 3c). For each individual trajectory, we can compute the associated square displacement $\text{SD}(t) = (X(t) - X(t=0))^2$, which characterizes the diffusive character of these random walks. From the initial increase of the square displacement with time, one can extract a diffusion coefficient D for each individual trajectory, as $\text{SD} = 4.D.t$ (dashed line in the SD graphs), which is found to be $D_{(a)} \approx 10^{-16} \text{ m}^2 \text{ s}^{-1}$ (no diffusion), $D_{(b)} \approx 8 \times 10^{-14} \text{ m}^2 \text{ s}^{-1}$ and $D_{(c)} \approx 25 \times 10^{-14} \text{ m}^2 \text{ s}^{-1}$, respectively. Note that the larger number of observed trajectories at the edges might be due to a larger density of defects (see Supplementary Fig. 27).

As shown in Fig. 4a, we characterize the interfacial mobility of protons at the surface of the flake through the evolution of the mean square displacement (MSD) averaged over all observed trajectories (the averaged $\text{MSD} = \langle (X(t) - X(t=0))^2 \rangle$ is a well-defined quantity, independent of sampling time and tracking parameters, see Supplementary Discussion 3). As shown in Fig. 4a, the MSD follows an initial linear increase, characteristic of a standard diffusive behaviour at short times ($t < 300$ ms), followed by a subdiffusive behaviour at longer times, which is possibly due to longer adsorbing events at some defect sites. The linear regime allows us to define the average diffusion coefficient $D = 2.8 \times 10^{-14} \text{ m}^2 \text{ s}^{-1}$, and is typically found to be of the order of $10^{-14} \text{ m}^2 \text{ s}^{-1}$ for the majority of flakes. We further show, in the inset, the broad distribution of

diffusion coefficients from individual single-molecule trajectories, with a noticeable proportion of trajectories characterized by no net observed motion ($D < 1 \times 10^{-16} \text{ m}^2 \text{ s}^{-1}$, as in Fig. 3a). To analyse the statistics of these bidimensional proton walks in more detail, we plot in Fig. 4b,c the distribution of hopping length δl and residence time T_R at the surface (calculated as $T_R = N_R \Delta t$, where N_R is the trajectory length in frames and the sampling time $\Delta t = 20$ ms). Those distributions are well approximated by power laws, $N(\delta l) \approx \delta l^{-\nu}$ and $N(T_R) \approx T_R^{-\mu}$, with values of $\nu \approx 2.6$ and $\mu \approx 1.6$ in this case, and values that are found typically in the range $\nu \in [2.4 - 4]$ and $\mu \in [1.6 - 2.5]$ (Supplementary Fig. 13). The power-law scaling for the jump length δl is reminiscent of Levy-type processes^{42,43}, and demonstrates the anomalous non-Brownian character of these hopping events, due to the finite distance between randomly distributed defects (defect density on this flake can be estimated to be at least $500 \mu\text{m}^{-2}$, leading to an averaged interdefect distance of 40 nm). The power-law scaling of the residence time naturally arises from the length of a diffusion-controlled escape process, and is larger than for normal diffusion, for which $\mu = 1.5$. Importantly, a large fraction ($\sim 70\%$) of protons remains on the surface of the flakes between each frame, leading to trajectories that are subsequently analysed (Supplementary Fig. 20).

The orders of magnitude difference between the measured diffusion coefficient for proton surface transport, $D \approx 10^{-14} \text{ m}^2 \text{ s}^{-1}$, and the hydronium diffusion coefficient in the bulk^{2,35,44}, $D_{\text{bulk}} \approx 10^{-8} - 10^{-7} \text{ m}^2 \text{ s}^{-1}$, and at biological membranes^{10–12}, $D_{\text{membrane}} \approx 10^{-11} - 10^{-9} \text{ m}^2 \text{ s}^{-1}$, suggests the presence of a strong rate-limiting step for interfacial proton transport. We thus compare the surface transport of the two isotopes, hydrogen and deuterium (Fig. 4d, comparing transport in H_2O and D_2O in a distinct flake, see also Supplementary Fig. 22). As shown in Fig. 4d, diffusion is hindered in D_2O by at least a factor of 4 compared with H_2O . This isotopic hindrance to diffusion is larger than the factor of 1.5–2 that one would expect from hindrance of either Grotthuss-like proton transfer or self-diffusion^{45,46}, pointing to desorption from defects rather than transport between nearby defects as the rate-limiting step for excess proton transport. Such desorption-limited transport is consistent with the low value of the interfacial diffusion coefficient, the large distribution in diffusion coefficients observed in individual trajectories (Fig. 4a, inset), as well as the long adsorbing steps

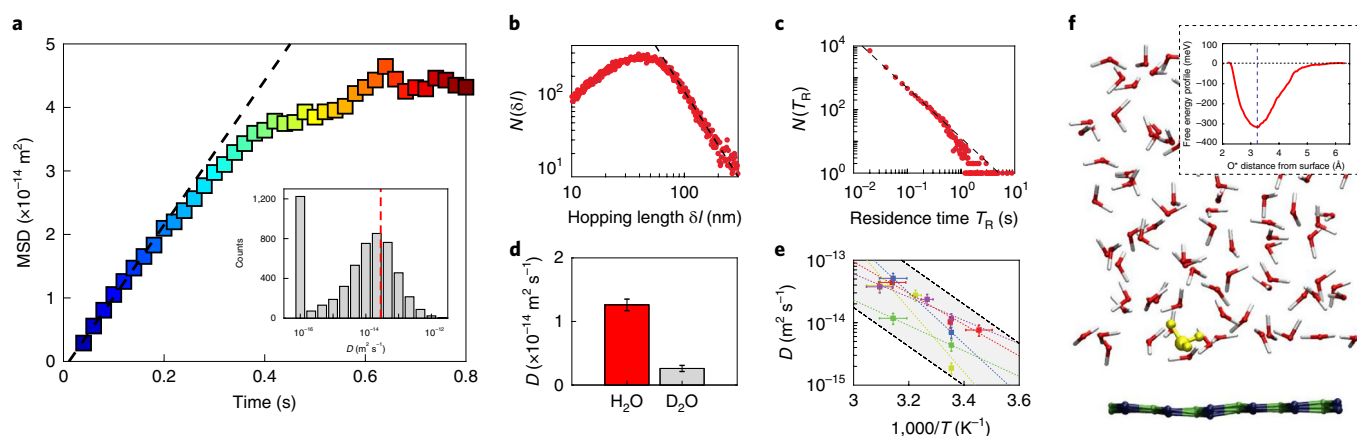


Fig. 4 | Mobility and segregation of protons at interfaces. **a**, Variation of the mean square displacement (MSD) as a function of time for the flake in Fig. 3. Dashed line is a linear fit from which we extract the averaged diffusion coefficient $D = 2.8 \times 10^{-14} \text{ m}^2 \text{ s}^{-1}$. Inset shows the distribution of the diffusion coefficient determined on individual trajectories, with the vertical dashed line being the averaged diffusion coefficient. **b**, Distribution of step length δl between successive jumps. Dashed line is a power-law fit with exponent $\nu \approx 2.6$. **c**, Distribution of residence time T_R . Dashed line is a power-law fit with exponent $\mu \approx 1.6$. **d**, Isotope effect, comparing diffusion coefficient in D_2O and H_2O in a distinct flake. Error bars represent standard deviation in the diffusion coefficient. **e**, Variation of diffusion coefficients as a function of inverse temperature for five distinct flakes, with linear fits shown as dashed coloured lines. Black dashed lines are visual guides showing activated Arrhenius behaviour with the mean activation energy of 0.62 eV (see Supplementary Fig. 28). **f**, Simulation snapshot of the trajectory of an aqueous hydronium ion physisorbed at the pristine hBN/water interface (see Supplementary Video 9). Inset shows the computed free-energy profile of the hydronium ion as it approaches the hBN layer, with a physisorption well of -0.3 eV centred around the maximum of water density at 3.3 Å (blue vertical dotted line in inset, see Supplementary Discussion 5).

evidenced at some defect sites (Fig. 3, trajectories (a) and (c)). Note, finally, that this hindered desorption-limited transport validates a posteriori the choice of our spatiotemporal resolution and tracking parameters ($\Delta t = 10 - 20 \text{ ms}$ and $\Delta l = 300 \text{ nm}$) for which the largest measurable diffusion coefficient is $\Delta l^2 / 4\Delta t \approx 10^{-12} \text{ m}^2 \text{ s}^{-1}$. This value, despite being smaller than the bulk hydronium diffusion coefficients, remains two orders of magnitude larger than the desorption-limited interfacial diffusivities, allowing us to consistently measure and characterize the hindered interfacial proton transport between defects (Supplementary Discussion 3). Additional characterization of the proton transit time between defects (corresponding to unhindered interfacial proton transport) would require a temporal resolution $\delta t \approx 1 \mu\text{s}$ at this 100-nm scale, which is unreachable even with state-of-the-art single-molecule tracking techniques⁴⁷.

On the basis of these insights, we can, for desorption-limited transport, express the diffusion coefficient as $D = \frac{1}{4}\Gamma a^2$, with $\Gamma \text{ (s}^{-1}\text{)}$ the jump rate and a the characteristic jump length between nearby defects. This jump rate scales as $\Gamma \approx \nu \exp\left(\frac{-\Delta F}{k_B T}\right)$, where $\nu \text{ (s}^{-1}\text{)}$ is a molecular frequency and ΔF is the free-energy desorption barrier from the defect⁴⁸. As an order of magnitude estimate, we take the attempt frequency as $\nu \approx 1/\tau$, with τ of the order of nanoseconds corresponding to the excited-state lifetime⁴⁹ (Supplementary Fig. 2), and $a \approx 10 - 100 \text{ nm}$, leading to a typical desorption energy barrier of $16 - 20 k_B T \approx 0.4 - 0.5 \text{ eV}$. As shown in Fig. 4e, we indeed observe an increase in proton mobility with increasing temperature, from which we extract a mean activation energy $\Delta E \approx 0.62 \pm 0.12 \text{ eV}$, demonstrating the predominantly enthalpic nature of this free-energy barrier (Supplementary Fig. 28). This barrier then characterizes the energy necessary to break the NH covalent bond from the excited defect $\text{V}_B^+ \text{H}$ and for the solvated H^+ to escape the electrostatic attraction of the negatively charged vacancy V_B^- . Consistently, this barrier is much smaller than the hydrogen removal energy of $> 2.34 \text{ eV}$ predicted to break the NH bond from the $\text{V}_B \text{H}$ defect in gas phase³⁵, as the proton desorption barrier might be reduced here by the presence of nearby hydrogen-accepting water molecules, as well as by the laser irradiation. Indeed, we did not observe any

proton mobility in air (Supplementary Fig. 26), despite the presence of adsorbed water at the flake surface in ambient conditions (40% relative humidity), demonstrating the crucial role of bulk water in mediating proton mobility at the surface of the flake and consistent with recent simulations⁶. Desorption-limited transport is further confirmed by the weak dependence of mobility on illumination power (Supplementary Fig. 21). Furthermore, as shown in Supplementary Figs. 23 and 24, the presence of salt and dissolved gas does not noticeably affect the interfacial proton mobility, while we observed a net increase in mobility at low pH in a majority of flakes (Supplementary Fig. 25), consistent with increased defect activity and change of surface state. Finally, we note that the high purity and atomic flatness of the hBN surfaces should also lead to reduced probability of proton trapping at non-emissive sites, allowing direct observation of excess proton transport between nearby defects.

Proton segregation at the solid/water interface

The emerging picture is therefore that of a desorption-limited transport of protons between adjacent surface defects, mediated by the solid/water interface. While several experiments have reported evidence for interfacial proton mobility at surfaces through ensemble measurements^{9-12,50}, the trajectories observed here at the surface of the flake (Figs. 2 and 3) represent direct observation at the single-molecule scale of the interfacial segregation of proton excess at the solid/water interface, demonstrating that this interface provides a preferential pathway for charge transport. Indeed, in the absence of any free-energy barrier trapping protons at the interface, a proton irreversibly desorbing into the bulk would diffuse over $\delta l \approx \sqrt{D_{\text{bulk}} \cdot \delta t} \approx 300 \mu\text{m}$ during the $\delta t = 20 \text{ ms}$ sampling time, preventing any correlations in the activation of defects $\sim 100 \text{ nm}$ apart. The power-law tail of the surface residence time (Fig. 4c), concomitant with the finite diffusivity (Fig. 4a), accordingly demonstrates the large probability of near-surface charges remaining segregated and mobile at the surface. In-plane proton transport at the flake surface (Fig. 2c, step (ii)) must therefore be favoured compared to irreversible proton desorption into the bulk (Fig. 2c, step (iii)), due to the presence of an interfacial free-energy barrier leading to segregation of the excess protons at the hBN/water interface.

To probe the segregation of interfacial protons in more detail, we simulated the dynamics of a hydronium ion at the interface of water and pristine hBN (Fig. 4f). As observed in this 20-ps trajectory (Supplementary Video 9), the hydronium ion indeed remains segregated (physisorbed) at the interface, while keeping high lateral mobility through Grotthuss transfer, with a lateral diffusion coefficient $D \approx 8 \times 10^{-9} \text{ m}^2 \text{ s}^{-1}$ that is close to the bulk hydronium diffusion coefficient^{23,35,44} $D_{\text{bulk}} \approx 10^{-8} - 10^{-7} \text{ m}^2 \text{ s}^{-1}$. As shown in the inset of Fig. 4f, computation of the free energy of the aqueous hydronium approaching a pristine hBN surface further confirms the presence of an interfacial -0.3 eV physisorption well (Supplementary Discussion 5). Mechanistically, several effects can be invoked to explain the observed affinity of protons to interfaces. First, in hydronium ions, asymmetric charge distribution leads to an amphiphilic surfactant-like character^{12,51}, which could lead to segregation due to the hydrophobic nature of the hBN interface. Second, the ionic nature of the insulating hBN crystal⁵² could also be responsible for electrostatic trapping of the positively charged hydronium ion. Third, as hydronium donates three hydrogen bonds to water, this leads to straining and disruption of the hydrogen-bonding network⁵³. This effect is reduced at interfaces—at which the hydronium oxygen tends to point away from water⁴⁸—and could lead to trapping of the ion^{10,12,50,53}. Note that although these simulations suggest that surface proton transport is characterized by purely bidimensional diffusion at the solid/water interface, measuring whether this is actually the case in our experiments would require detailed analysis of the statistical properties of the proton transit time between adjacent defects⁵⁰. At this 100-nm scale, such measurements would require a temporal resolution of $\delta t \approx 1 \mu\text{s}$, which is unfortunately unattainable with current state-of-the-art single-molecule tracking techniques⁴⁷.

Conclusion

The combination of super-resolution microscopy and single-particle tracking on hBN defects allowed us to reveal proton trajectories between adjacent surface defects at the single-molecule scale. These observations establish that the solid/water interface provides a preferential pathway for proton transport, with excess protons remaining segregated at the surface, leading to the observed spatiotemporal correlations in the activation of nearby defects. The direct observation of this interfacial proton pathway has broad implications for charge transport in a range of fields and materials, and suggests that tuning of defect densities, binding affinities and illumination could allow the optimization and control of interfacial proton transport. Our experiments thus represent a promising platform for the investigation of proton transport at the single-molecule scale, opening up a number of avenues, for example, related to the interplay of flow or confinement with molecular charge transport at liquid/solid interfaces.

Online content

Any methods, additional references, Nature Research reporting summaries, source data, extended data, supplementary information, acknowledgements, peer review information; details of author contributions and competing interests; and statements of data and code availability are available at <https://doi.org/10.1038/s41565-020-0695-4>.

Received: 2 December 2019; Accepted: 16 April 2020;

Published online: 25 May 2020

References

- Kreuer, K. D. Proton conductivity: materials and applications. *Chem. Mater.* **8**, 610–641 (1996).
- Chen, M. et al. Hydroxide diffuses slower than hydronium in water because its solvated structure inhibits correlated proton transfer. *Nat. Chem.* **10**, 413–419 (2018).
- Reider, G., Höfer, U. & Heinz, T. Surface diffusion of hydrogen on Si (111)7×7. *Phys. Rev. Lett.* **66**, 1994–1997 (1991).
- Merte, L. R. et al. Water-mediated proton hopping on an iron oxide surface. *Science* **336**, 889–893 (2012).
- Kumagai, T. et al. H-atom relay reactions in real space. *Nat. Mater.* **11**, 167–172 (2012).
- Tocci, G. & Michaelides, A. Solvent-induced proton hopping at a water-oxide interface. *J. Phys. Chem. Lett.* **5**, 474–480 (2014).
- Nagasaka, M., Kondoh, H., Amemiya, K., Ohta, T. & Iwasawa, Y. Proton transfer in a two-dimensional hydrogen-bonding network: water and hydroxyl on a Pt(111) surface. *Phys. Rev. Lett.* **100**, 8–11 (2008).
- Grosjean, B., Bocquet, M. L. & Vuilleumier, R. Versatile electrification of two-dimensional nanomaterials in water. *Nat. Commun.* **10**, 1656 (2019).
- Bränden, M., Sanden, T., Brzezinski, P. & Widengren, J. Localized proton microcircuits at the biological membrane–water interface. *Proc. Natl Acad. Sci. USA* **103**, 19766–19770 (2006).
- Cherepanov, D. A., Pohl, P., Hagen, V., Antonenko, Y. N. & Springer, A. Protons migrate along interfacial water without significant contributions from jumps between ionizable groups on the membrane surface. *Proc. Natl Acad. Sci. USA* **108**, 14461–14466 (2011).
- Serowy, S. et al. Structural proton diffusion along lipid bilayers. *Biophys. J.* **84**, 1031–1037 (2003).
- Zhang, C. et al. Water at hydrophobic interfaces delays proton surface-to-bulk transfer and provides a pathway for lateral proton diffusion. *Proc. Natl Acad. Sci. USA* **109**, 9744–9749 (2012).
- Karim, W. et al. Catalyst support effects on hydrogen spillover. *Nature* **541**, 68–71 (2017).
- Michaelides, A. & Hu, P. Catalytic water formation on platinum: a first-principles study. *J. Am. Chem. Soc.* **123**, 4235–4242 (2001).
- Cortright, R. D., Davda, R. R. & Dumesic, J. A. Hydrogen from catalytic reforming of biomass-derived hydrocarbons in liquid water. *Nature* **418**, 964–967 (2002).
- Schmidt-Rohr, K. & Chen, Q. Parallel cylindrical water nanochannels in Nafion fuel-cell membranes. *Nat. Mater.* **7**, 75–83 (2008).
- Hickner, M. A., Ghassemi, H., Kim, Y. S., Einsla, B. R. & McGrath, J. E. Alternative polymer systems for proton exchange membranes (PEMs). *Chem. Rev.* **104**, 4587–4612 (2004).
- Kreuer, K.-D., Paddison, S. J., Spohr, E. & Schuster, M. Transport in proton conductors for fuel-cell applications: simulations, elementary reactions, and phenomenology. *Chem. Rev.* **104**, 4637–4678 (2004).
- Ling, X., Bonn, M., Domke, K. F. & Parekh, S. H. Correlated interfacial water transport and proton conductivity in perfluorosulfonic acid membranes. *Proc. Natl Acad. Sci. USA* **116**, 8715–8720 (2019).
- Boysen, D. A., Uda, T., Chisholm, C. R. I. & Haile, S. M. High-performance solid acid fuel cells through humidity stabilization. *Science* **303**, 68–70 (2004).
- Gopinadhan, K. et al. Complete steric exclusion of ions and proton transport through confined monolayer water. *Science* **363**, 145–148 (2019).
- Lee, C. Y., Choi, W., Han, J.-H. & Strano, M. S. Coherence resonance in a single-walled carbon nanotube ion channel. *Science* **329**, 1320–1324 (2010).
- Tunuguntla, R. H. et al. Enhanced water permeability and tunable ion selectivity in subnanometer carbon nanotube porins. *Science* **357**, 792–796 (2017).
- Zhou, K. G. et al. Electrically controlled water permeation through graphene oxide membranes. *Nature* **559**, 236–240 (2018).
- Feng, J. et al. Imaging of optically active defects with nanometer resolution. *Nano Lett.* **18**, 1739–1744 (2018).
- Comtet, J. et al. Wide-field spectral super-resolution mapping of optically active defects in hexagonal boron nitride. *Nano Lett.* **19**, 2516–2523 (2019).
- Freier, E., Wolf, S. & Gerwert, K. Proton transfer via a transient linear water-molecule chain in a membrane protein. *Proc. Natl Acad. Sci. USA* **108**, 11435–11439 (2011).
- Wendt, S. et al. Formation and splitting of paired hydroxyl groups on reduced TiO₂. *Phys. Rev. Lett.* **96**, 066107 (2006).
- Taniguchi, T. & Watanabe, K. Synthesis of high-purity boron nitride single crystals under high pressure by using Ba-BN solvent. *J. Cryst. Growth* **303**, 525–529 (2007).
- Léonard, S., Ingrid, S., Frédéric, F., Annick, L. & Julien, B. Characterization methods dedicated to nanometer-thick hBN layers. *2D Mater.* **4**, 15028 (2017).
- Vogl, T., Campbell, G., Buchler, B. C., Lu, Y. & Lam, P. K. Fabrication and deterministic transfer of high-quality quantum emitters in hexagonal boron nitride. *ACS Photonics* **5**, 2305–2312 (2018).
- Martínez, L. J. et al. Efficient single photon emission from a high-purity hexagonal boron nitride crystal. *Phys. Rev. B* **94**, 121405 (2016).
- Weston, L., Wickramaratne, D., Macko, M., Alkauskas, A. & Van De Walle, C. G. Native point defects and impurities in hexagonal boron nitride. *Phys. Rev. B* **97**, 214104 (2018).
- Wang, Q. et al. Photoluminescence upconversion by defects in hexagonal boron nitride. *Nano Lett.* **18**, 6898–6905 (2018).

35. Agmon, N. Elementary steps in excited-state proton transfer. *J. Phys. Chem. A* **109**, 13–35 (2005).
36. Scharnagl, C., Raupp-Kossmann, R. & Fischer, S. F. Molecular basis for pH sensitivity and proton transfer in green fluorescent protein: protonation and conformational substates from electrostatic calculations. *Biophys. J.* **77**, 1839–1857 (1999).
37. Habuchi, S. et al. Photo-induced protonation/deprotonation in the GFP-like fluorescent protein Dronpa: mechanism responsible for the reversible photoswitching. *Photochem. Photobiol. Sci.* **5**, 567–576 (2006).
38. Janssen, K. P. F. et al. Single molecule methods for the study of catalysis: from enzymes to heterogeneous catalysts. *Chem. Soc. Rev.* **43**, 990–1006 (2014).
39. Roeffaers, M. B. J. et al. Spatially resolved observation of crystal-face-dependent catalysis by single turnover counting. *Nature* **439**, 572–575 (2006).
40. Zou, N. et al. Cooperative communication within and between single nanocatalysts. *Nat. Chem.* **10**, 607–614 (2018).
41. Manley, S. et al. High-density mapping of single-molecule trajectories with photoactivated localization microscopy. *Nat. Methods* **5**, 155–157 (2008).
42. Bouchaud, J. P., Comtet, A., Georges, A. & Le Doussal, P. Classical diffusion of a particle in a one-dimensional random force field. *Ann. Phys.* **201**, 285–341 (1990).
43. Zhaburdaev, V., Denisov, S. & Klafter, J. Lévy walks. *Rev. Mod. Phys.* **87**, 483–530 (2015).
44. Heberle, J., Riesle, J., Thiedemann, G., Oesterhelt, D. & Dencher, N. A. Proton migration along the membrane surface and retarded surface to bulk transfer. *Nature* **370**, 379–382 (1994).
45. Halle, B. & Karlström, G. Prototropic charge migration in water. *J. Chem. Soc. Faraday Trans.* **79**, 1047–1073 (1983).
46. Sluyters, J. H. & Sluyters-Rehbach, M. The mechanism of the hydrogen ion conduction in liquid light and heavy water derived from the temperature dependence of their limiting conductivities. *J. Phys. Chem. B* **114**, 15582–15589 (2010).
47. Eilers, Y., Ta, H., Gwosch, K. C., Balzarotti, F. & Hell, S. W. MINFLUX monitors rapid molecular jumps with superior spatiotemporal resolution. *Proc. Natl Acad. Sci. USA* **115**, 6117–6122 (2018).
48. Reed, D. A. & Ehrlich, G. Surface diffusion, atomic jump rates and thermodynamics. *Surf. Sci.* **102**, 588–609 (1981).
49. Tran, T. T., Bray, K., Ford, M. J., Toth, M. & Aharonovich, I. Quantum emission from hexagonal boron nitride monolayers. *Nat. Nanotechnol.* **11**, 37–41 (2016).
50. Weichselbaum, E. et al. Origin of proton affinity to membrane/water interfaces. *Sci. Rep.* **7**, 1–8 (2017).
51. Kudin, K. N. & Car, R. Why are water-hydrophobic interfaces charged? *J. Am. Chem. Soc.* **130**, 3915–3919 (2008).
52. Tocci, G., Joly, L. & Michaelides, A. Friction of water on graphene and hexagonal boron nitride from ab initio methods: very different slippage despite very similar interface structures. *Nano Lett.* **14**, 6872–6877 (2014).
53. Dellago, C. & Hummer, G. Kinetics and mechanism of proton transport across membrane nanopores. *Phys. Rev. Lett.* **97**, 1–4 (2006).

Publisher's note Springer Nature remains neutral with regard to jurisdictional claims in published maps and institutional affiliations.

© The Author(s), under exclusive licence to Springer Nature Limited 2020

Data availability

The data that support the findings of this study are available from the corresponding authors on reasonable request.

Acknowledgements

J.C. acknowledges valuable discussions with A. Descloux and V. Navikas. This work was financially supported by the Swiss National Science Foundation Consolidator grant (BIONIC BSCG10_157802) and CCMX project (Large area growth of 2D materials for device integration). E.G. acknowledges support from the Swiss National Science Foundation through the National Centre of Competence in Research Bio-Inspired Materials. The quantum simulation work was performed on the French national supercomputer Occigen under DARI grants A0030807364 and A0030802309. M.-L.B. acknowledges funding from ANR project Neptune. K.W. and T.T. acknowledge support from the Elemental Strategy Initiative conducted by MEXT, Japan, and CREST (JPMJCR15F3), JST.

Author contributions

J.C. and A.R. conceived and designed the experiments and J.C. performed the experiments with help from E.G. and A.A. J.C. analysed data and wrote the paper, with

input from all authors. B.G. carried out simulations, with help from R.V. and M.-L.B. and K.W. and T.T. contributed materials. A.R. supervised the project. All authors discussed the results and commented on the manuscript.

Competing interests

The authors declare no competing interests.

Additional information

Supplementary information is available for this paper at <https://doi.org/10.1038/s41565-020-0695-4>.

Correspondence and requests for materials should be addressed to J.C. or A.R.

Peer review information *Nature Nanotechnology* thanks Johan Hofkens, Peter Pohl and the other, anonymous, reviewer(s) for their contribution to the peer review of this work.

Reprints and permissions information is available at www.nature.com/reprints.